

Efficient Light Field Reconstruction via Spatio-Angular Dense Network

Zexi Hu^{ID}, Henry Wing Fung Yeung^{ID}, Xiaoming Chen^{ID}, Yuk Ying Chung^{ID}, Member, IEEE, and Haisheng Li^{ID}

Abstract—As an image sensing instrument, light field images can supply extra angular information compared with monocular images and have facilitated a wide range of measurement applications. Light field image capturing devices usually suffer from the inherent tradeoff between the angular and spatial resolutions. To tackle this problem, several methods, such as light field reconstruction and light field super-resolution, have been proposed but leaving two problems unaddressed, namely domain asymmetry and efficient information flow. In this article, we propose an end-to-end spatio-angular dense network (SADenseNet) for light field reconstruction with two novel components, namely correlation blocks and spatio-angular dense skip connections to address them. The former performs effective modeling of the correlation information in a way that conforms with the domain asymmetry. Also, the latter consists of three kinds of connections enhancing the information flow within two domains. Extensive experiments on both real-world and synthetic datasets have been conducted to demonstrate that the proposed SADenseNet’s state-of-the-art performance at significantly reduced costs in memory and computation. The qualitative results show that the reconstructed light field images are sharp with correct details and can serve as preprocessing to improve the accuracy of related measurement applications.

Index Terms—Convolutional neural network, deep learning, image processing, light field (LF) imaging, light field reconstruction.

I. INTRODUCTION

AS AN emerging image sensing instrument, light field (LF) cameras can capture a set of images from different perspectives. This feature offers advantages in

Manuscript received April 14, 2021; revised June 19, 2021; accepted July 10, 2021. Date of publication July 26, 2021; date of current version August 17, 2021. This work was supported in part by National Natural Science Foundation of China under Grant 62177001 and Grant 61877002, in part by Beijing Natural Science Foundation and Fengtai Rail Transit Frontier Research Joint Fund under Grant L191009, in part by Scientific Research Program of Beijing Municipal Education Commission under Grant KZ202110011017, and in part by Research Foundation for Advanced Talents of Beijing Technology and Business University under Grant 19008021181. The Associate Editor coordinating the review process was Dr. Yan Zhuang. (*Corresponding author: Xiaoming Chen*)

Zexi Hu is with the School of Computer Science and Engineering, Beijing Technology and Business University, Beijing 100048, China, and also with the School of Computer Science, University of Sydney, Sydney, NSW 2006, Australia (e-mail: zexi.hu@sydney.edu.au).

Henry Wing Fung Yeung and Yuk Ying Chung are with the School of Computer Science, University of Sydney, Sydney, NSW 2006, Australia (e-mail: henrywfyueung@gmail.com; vera.chung@sydney.edu.au).

Xiaoming Chen and Haisheng Li are with the School of Computer Science and Engineering, Beijing Technology and Business University, Beijing 100048, China (e-mail: xiaoming.chen@btbu.edu.cn; lihsh@btbu.edu.cn).

Digital Object Identifier 10.1109/TIM.2021.3100326

vision-based measurement tasks. For example, researchers proposed using LF camera [1]–[4] for more accurate face detection that is more robust to spoof attacks. Similar achievement in measurement accuracy has been seen in material recognition [5], [6] where the subjects cannot be easily distinguished in regular 2-D images [7] and salient object detection in complex scenarios [8], [9]. The abundant information provided by LF instruments also facilitates depth measurement and 3-D measurement with promising accuracy [10]–[13] compared with other types of image sensors, such as stereo vision [14] and structured light [15]. The emergence of LF cameras, e.g., Raytrix R series [16], [17] and Lytro Illum [18], has enabled LF instruments to apply to a wide range of consumer- and industrial-grade applications, such as measurement in industrial quality control [17], [19]. However, due to the limited capacity of microlens inside the sensor, these cameras inherently suffer from a low resolution and a tradeoff between the angular and spatial resolutions.

For mitigating the tradeoff, there are two major solutions, namely LF reconstruction and LF spatial super-resolution (LFSR). The former focuses on upsampling in the angular domain, i.e., the number of sub-aperture images (SAI), whereas the latter aims at increasing the resolution of the spatial domain, i.e., the spatial resolution of each SAI. This article focuses on the former category to reconstruct a densely sampled LF from a sparsely sampled one. With the recent success of deep learning in image processing, learning-based methods are also introduced to LF reconstruction and have achieved superior performance [20], [21]. However, these methods still suffer from problematic spatio-angular features extraction, which limits their performance. It stems from two aspects, namely *domain asymmetry* and *inefficient information flow*.

Regarding *domain asymmetry*, it has been discovered in [22] that the information in the spatial and angular domains has distinct natures as the spatial domain contains the regular 2-D image information, whereas the angular domain encodes the disparity information between the adjacent SAIs. It is also obvious that these two domains are spaces of enormously different sizes. Specifically, given an LF image $X \in \mathbb{R}^{U \times V \times W \times H}$, the spatial space $W \times H$ is usually much larger than the angular space $U \times V$, i.e., $U \times V \ll W \times H$. This issue becomes more prominent in LF reconstruction where the high-frequency information in the angular domain is largely damaged when downsampling into the sparsely sampled LF image. In other words, the angular domain becomes further smaller and sparser. Therefore, it is unreasonable to process

the two domains, which are asymmetrical in natures and volumes, in the same manner. Still, the existing methods manipulate the 4-D LF data in a symmetrical manner. These methods majorly fall into three categories: 4-D convolution filters [21], [23], epipolar-plane images (EPI)-based methods [10], [22], [24]–[27], and pseudo-4-D convolution filters [5], [21], [23].

A 4-D convolution filter processes the LF image straightforwardly as it convolves the spatial and angular domains simultaneously. However, it is proven to be inefficient as it requires expensive computation and large memory consumption [5], [21]. As an alternative, the EPI-based methods have been proposed, which perform independent super-resolution on EPI slices. An EPI slice can be obtained from the 4-D LF by fixing two specific coordinates, with one lying on the spatial domain and the other on the angular domain. An illustration of this idea is shown in Fig. 1(a). As EPI slices are essentially 2-D images with patterns that reflect the correlation information in the LF image, these methods decompose the 4-D LF reconstruction task into a series of 2-D subtasks. Another alternative is pseudo-4-D convolution filters that decompose a 4-D convolution into a spatial and an angular convolution separately. Typical examples are the interleaved 2-D angular and spatial convolutions to simulate 4-D filters for material recognition [5] and the spatio-angular separable (SAS) convolution for LF reconstruction and super-resolution [21], [23]. Illustrations of EPI-based and pseudo-4-D methods are shown in Fig. 1(b) and (c), respectively.

Even though the aforementioned three options have achieved remarkable progress in extracting spatio-angular features, the vast majority of them treat the spatial and angular dimensions symmetrically against the domain asymmetry. One of the very few exceptions is [22] where the issue was addressed by its “blur-restoration-deblur” framework, which downsamples the spatial domain for conforming with the asymmetry at the expense of losing spatial high-frequency information rendering the method suboptimal. In this article, we argue that the operations performed in the spatial and angular domains should be of distinct natures accordingly. The convolution operation performed in the spatial domain is modeling the local spatial features such as edges and corners, whereas the one performed in the angular domain is modeling the disparities information. Therefore, we have hypothesized that the symmetrical pattern hampers the spatioangular feature representation and we proposed *correlation blocks* that comprise an uneven number of spatial and angular convolutions to model correlation information of LF images asymmetrically. Unlike [22], our approach does not involve any downsampling or other operations that would explicitly abandon any valuable information in any domain but fully convolves on both domains. We elaborate this component in Section III-B and validate our hypothesis in the ablation study in Section IV-D2.

As for *inefficient information flow*, most computer vision methods have suffered from it as they opted to increase network depth [28], [29] to extract deeper features. Obviously, its downside is a huge number of trainable parameters and high computation cost. The other defect is the gradient-vanishing

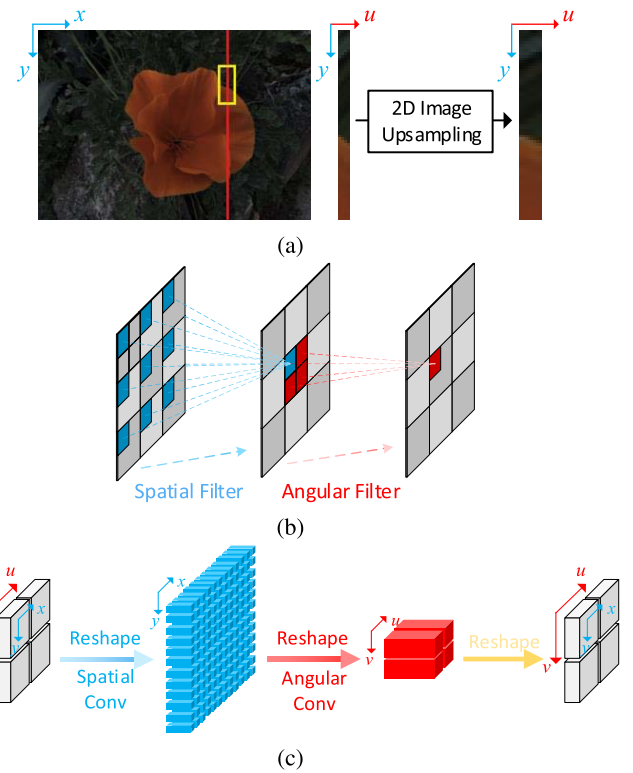


Fig. 1. Illustrations of the 4-D convolution alternatives. (a) EPI. (b) Interleaved 2-D convolution. (c) SAS convolution. They all process the spatio-angular information in a symmetrical way.

problem [30], especially in shallow layers, as networks go deeper, resulting in training difficulties. These negative effects can be amplified in the realm of LF images due to its 4-D high volume [5], [21], leading to model inefficiency when training and testing. For example, Yeung *et al.* [21] have proposed a network that outperforms Kalantari *et al.* [20] by 0.3 dB peak signal-to-noise ratio (PSNR) with four SAS convolutions. Yet, the performance gain is diminishing as more SAS convolutions are added, with a further 0.3 and 0.6 dB improvement at 8 and 16 SAS convolutions, which requires 1.5 and 2 times of model size, respectively. Although it has achieved state-of-the-art performance, the 16-SAS-convolution network contains around 1.5 million parameters and takes more than eight days to fully converge, rendering the model difficult to train and impractical to apply to memory-constrained devices.

Inspired by the success of dense skip connections that have been widely studied and exploited in image processing [30]–[34], we propose to use dense skip connections to enhance the information flow. Contrary to the previous dense networks, we propose spatio-angular dense skip connections specially designed for LF images that consist of three kinds of connections, namely angular, spatial, and image skip connections, to supply distinct types of information and reinforce the spatio-angular feature representation.

Finally, with these two components, correlation blocks and spatio-angular dense skip connections, we propose a simple yet efficient end-to-end spatio-angular dense network (SADenseNet). Extensive experiments are conducted on both real-world and synthetic datasets to demonstrate the

SADenseNet's superior performance of LF reconstruction at substantially lower computational and memory costs compared with state-of-the-art methods. A series of ablation studies are also presented to verify the proposed components' effectiveness, and we also perform SADenseNet as preprocessing that yields a positive effect for depth estimation to prove its potential for more accurate LF measurement application.

The major contributions of this article are summarized in the following five aspects.

- 1) Correlation blocks are proposed to model correlation information based on the study of domain asymmetry.
- 2) Spatio-angular dense skip connections are proposed to enhance the information flow within spatial and angular domains.
- 3) With the proposed components, we design a simple yet efficient end-to-end network, SADenseNet, for LF reconstruction.
- 4) SADenseNet is evaluated by extensive experiments on both real-world and synthetic datasets to verify its superior performance and efficiency in computation and memory usage compared with previous state-of-the-art methods.
- 5) An experiment on depth estimation is conducted to prove that SADenseNet can improve the accuracy of LF's measurement applications.

II. RELATED WORKS

A. LF Image Processing

To process LF images, early methods [35]–[37] explicitly estimate the disparity or depth and then obtain the reconstructed SAIs by warping the input SAIs and blending. Various depth estimation methods are proposed, e.g., phase-based estimation [36] and EPI-based estimation [37]. Different blending methods are also introduced, e.g., soft blending [38] and learning-based blending [39]. These methods are overly dependent on the quality of the disparity or depth maps in which the existence of noise in them causes undesirable artifacts. Such approaches are also disadvantaged when handling occluded areas as the warping process has no information about the invisible parts.

In recent years, significant progress in computer vision has been achieved by the deep learning-based methods [28], [32], [40], [41], and this technique has been applied to LF reconstruction. The first deep learning-based LF reconstruction method has been proposed by Kalantari *et al.* [20], which designed a disparity network to estimate the disparity and reconstruct the intermediate SAIs by warping the input SAIs with the calculated disparity. After that, the input and intermediate SAIs are fed into a color network to obtain the refined SAIs. This method has achieved outstanding performance with the deep features extracted by the deep neural networks. However, the reconstruction quality is limited due to the artifacts brought by the explicit disparity estimation and warping process. Moreover, each SAI needs to be individually reconstructed, which leads to duplicated calculations. Similarly, Zhou *et al.* [42] proposed an encoder-decoder network to estimate the disparity to synthesize views by warping.

With the help of its modified ResNet-50 to extract expressive representation and three subnetworks for disparity estimation, noise filtering, and view rendering, robustness is gained against input noise.

Wang *et al.* [27] proposed an EPI-based method to decompose the 4-D task into 3-D subtasks and train two networks separately for vertical and horizontal reconstructions. Heber *et al.* [10] and [26] designed a U-shaped network to extract shape information by EPIS, while Shin *et al.* [25] proposed an EPI-based method to compute disparity maps from LF with a four-branch network. A common drawback of EPI-based methods is that they ignore either one [25]–[27] or two dimensions [10], [22] of the 4-D LF in their optimization and cannot be jointly optimized in all dimensions. Therefore, they cannot process the LF data in a global scope.

Yeung *et al.* [21] proposed an end-to-end network that removes explicit disparity manipulation and reconstructs SAIs at a single forward propagation. This method has achieved groundbreaking performance with its SAS convolution that enables joint optimization in all dimensions. However, it has endured the same defect of stacking convolutional layers for obtaining deeper feature representation as other computer vision tasks [28], [43]. Different from decomposing 4-D convolution [21], Meng *et al.* [44] pursued to fully exploit high-dimensional LF information and proposed aperture group batch normalization to ease the training of 4-D convolutional network. In addition to pixel-wise loss function in the spatial space, they proposed an angular loss to optimize the error in the EPI space to preserve the correlation information of adjacent viewpoints. However, suffering from heavy 4-D convolution operations, it was still running at a large cost of computation and memory, and the high-dimensional information was yet to be fully exploited as the performance gain was not proportional to its costs. Besides pure learning-based methods, Chandramouli *et al.* [45] proposed a generative model to tackle the issue that learning-based models are confined to the observation model they have been trained on. Despite its limited performance, the fashion is inspiring with possibilities of LF models with generalization abilities.

There are some other methods [46], [47] that perform LF reconstruction but in a compressive manner. Their compression performance is proven to be promising, but they are essentially a different task from regular LF reconstruction as the full LF image is involved to be encoded into a small volume of information instead of a limited set of SAIs. Although the above methods and the regular LF reconstruction are not working in exactly the same application scenarios, it would be interesting to see where their performance ceilings are located.

In this article, our proposed SADenseNet has a similar pipeline as in [21] that contains two parts, namely the feature extraction and the SAI reconstruction. However, we ditch the refinement work as SADenseNet's feature extraction is so strong with the help of correlation blocks and spatio-angular dense skip connections that postprocessing components are unnecessary. Rather than inefficient explicit warping process [20] and costly 4-D convolution operations [44], we pursue the potential of decomposed convolution operations and information flow enhancement.

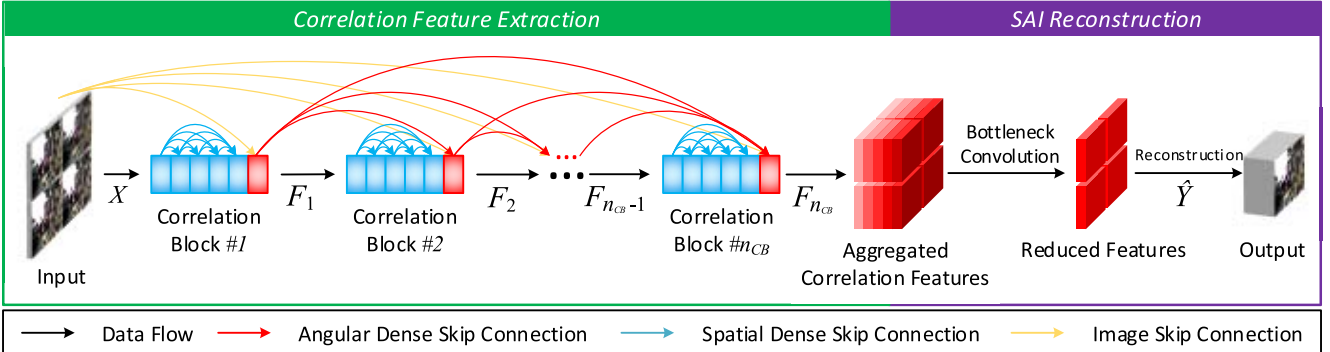


Fig. 2. Illustration of SADenseNet, which comprises two processes, namely correlation feature extraction and SAI reconstruction. The black arrows indicate the regular data flow and the colored arrows indicate dense skip connections. Red and blue arrows represent angular and spatial dense skip connections, respectively, and yellow ones represent image skip connections.

B. Feature Representation

In order to acquire powerful feature representation, stacking convolutional layers is the most straightforward solution since more parameters lead to higher nonlinearity and more complicated mapping functions. However, heavier computation costs and higher risks of overfitting are also incurred. To this end, some studies have discovered more efficient network structures.

The residual connection is one of the widely used structures first proposed by He *et al.* [48] to force layers to learn residue of a mapping function instead of the mapping function itself. Such a technique eases the optimization and improves the feature representation and can be applied to other computer vision tasks, such as single image super-resolution (SISR) [29], [49], [50] and visual tracking [51], [52].

On the other hand, dense skip connections have been proposed to mitigate the gradient-vanishing problem while aggregating hierarchical features of low and high frequencies [30]. Tai *et al.* [31] proposed a densely connected network to aggregate short- and long-term memories for image restoration. In SISR, Tong *et al.* [32] designed local and global dense skip connections to aid the feature extraction. Haris *et al.* [33] designed a projection unit to learn downsampling as well as upsampling. Li *et al.* [34] introduced feedback units containing projection groups to form a recurrent neural network (RNN) to enforce a curriculum learning strategy. The basic units of the latter two methods [33], [34] are reinforced with dense skip connections to gain richer feature representation. Among these, Tai *et al.* [31] and Tong *et al.* [32] have similar architectures with our SADenseNet as they perform dual dense skip connections. Nevertheless, the critical difference is that their duality is for extracting homogeneous features, while ours are for spatio-angular features from the two distinct domains.

C. Video-Related Tasks

Video-related tasks share similarities with LF tasks as they are both extracting cross-domain representation and processing multiple images or frames that are highly correlated with each other. A powerful spatiotemporal feature representation is a key to success as well. In terms of decomposition of high dimensions, similar methods can be found

in pseudo-3-D-based P3D [53], [54] and R2D [55]. Different from the pseudo-4-D convolution in LF, the pseudo-3-D convolutions decompose a 3-D convolution into two 2-D convolutions operating in the spatial and temporal spaces separately. Convolution decomposition has been proven to achieve better performance than the original 3-D convolution achieved by the extra nonlinearity and the reduced risk of overfitting.

III. PROPOSED METHOD

A. Overview

Let us consider $\mathcal{F}(X)$ as the LF reconstruction function that maps the input SAIs X to the reconstructed SAIs \hat{Y} , and hence,

$$\hat{Y} = \mathcal{F}(X) \quad X \in \mathbb{R}^{U \times V \times W \times H}, \quad \hat{Y} \in \mathbb{R}^{\mathcal{N} \times W \times H} \quad (1)$$

where (U, V) of X and \mathcal{N} of \hat{Y} denote the input and output angular resolution, respectively, i.e., the number of SAIs, while (W, H) is the spatial resolution, i.e., the resolution of every single SAI. The input SAIs X , which is a sparsely sampled LF image, and the reconstructed SAIs \hat{Y} can finally form a densely sampled LF image $\hat{I} \in \mathbb{R}^{\bar{U} \times \bar{V} \times W \times H}$. Therefore,

$$\bar{U} \times \bar{V} = U \times V + \mathcal{N}.$$

The objective of this article is to train an end-to-end network to learn $\mathcal{F}(X)$ in 1 for estimating \hat{Y} that approximates the ground truth Y . The proposed SADenseNet comprises two components, correlation feature extraction and SAI reconstruction, and an illustration is given in Fig. 2. The input SAIs X are fed into correlation feature extraction containing a series of correlation blocks, which will be described in Section III-B. In addition to the correlation blocks, spatio-angular dense skip connections are exploited through the inter- and intra-correlation blocks to enhance the information flow, which will be elaborated in Section III-C. With the extracted correlation features, SAI reconstruction will finally reconstruct SAIs \hat{Y} , which will be explained in Section III-D.

B. Correlation Blocks

For addressing the aforementioned domain asymmetry problem in Section I, we propose correlation blocks that process the

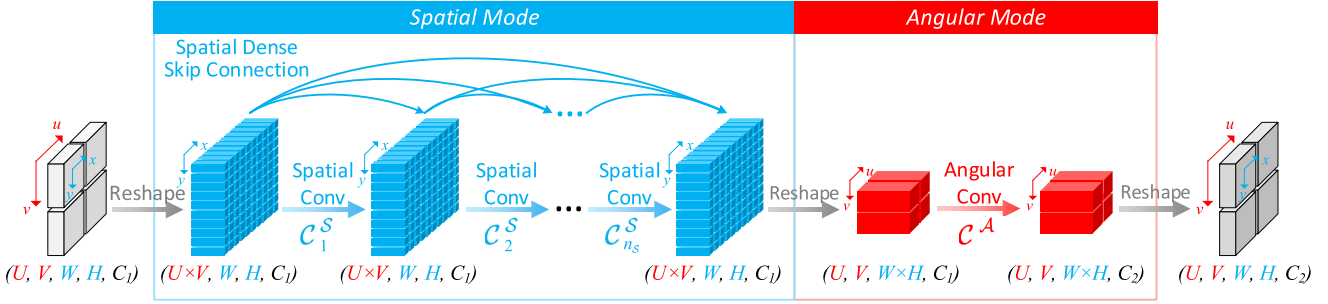


Fig. 3. Illustration of a correlation block. Blue tensors and arrows indicate tensors and operations under the spatial mode. Red counterparts indicate the angular ones likewise.

spatial and angular information asymmetrically. The structure is shown in Fig. 3.

The component is based on the SAS module proposed in [21] and [23]. However, motivated by the fact that the spatial space is usually substantially larger compared to the angular space, i.e., $U \times V \ll W \times H$, we presume that more spatial operations are needed than angular operations. Therefore, in each block, the 4-D LF tensor of size (U, V, W, H, C_1) , where C_1 is the number of input channels, is first reshaped into the spatial mode of size $(U \times V, W, H, C_1)$ to flatten the angular dimensions. Subsequently, a series of spatial convolutional layers, denoted as $[C_1^S, C_2^S, \dots, C_{nS}^S]$, are operated on the reshaped tensor of kernel size $(1, k_w, k_h, C_1, C_1)$ to extract the spatial features, where n_S is the number of spatial convolutional layers.¹ Likewise, the output of spatial convolution series is reshaped into the angular mode of size $(U, V, W \times H, C_1)$ and convolved by an angular convolutional layer of kernel size $(k_u, k_v, 1, C_1, C_2)$ to extract angular features that model the correlation information, where C_2 is the number of output channels. Finally, the tensor is reshaped back into the original shape with new channels (U, V, W, H, C_2) for the upcoming operation. Hence, a correlation block can be formulated as

$$\mathcal{H}(x) = \mathcal{A}(\mathcal{S}(x)) \quad (2)$$

$$\mathcal{A}(x) = \mathcal{C}^A(x) \quad (3)$$

$$\mathcal{S}(x) = \mathcal{C}_{nS}^S (\mathcal{C}_{nS-1}^S (\dots (\mathcal{C}_2^S (\mathcal{C}_1^S (x))) \dots)) \quad (4)$$

where \mathcal{S} and \mathcal{A} denote the spatial and angular feature extraction, respectively, and $\mathcal{C}^S(x)$ and $\mathcal{C}^A(x)$ denote the corresponding convolution functions.

Such an asymmetrical processing method suits LF image data compared with the existing 4-D convolution alternatives because the spatial information is sufficiently convolved to extract informative features with an enlarged receptive field in the spatial domain before the subsequent angular convolution.

In order to acquire deeper correlation features, a series of correlation blocks are employed consecutively as

$$F_i = \begin{cases} \mathcal{H}(F_{i-1}), & \text{if } i > 1 \\ \mathcal{H}(X), & \text{if } i = 1 \end{cases} \quad (5)$$

where F_i denotes the output tensor of i -th correlation block.

¹In this article, the last two values of the size of 3-D convolution kernels denote the input and output channels correspondingly.

The angular convolutions of correlation blocks are operated on the coarse-to-fine spatial features, and thus, they can extract correlation features hierarchically. The correlation extraction can be regarded as implicit disparity modeling but without explicit dependence on the accuracy of disparity. We denote the number of correlation blocks as n_{CB} and set both (k_u, k_v) and (k_w, k_h) to $(3, 3)$ across all the correlation blocks. Finally, the output of the last correlation block $F_{n_{CB}}$ will be fed to the following SAI reconstruction process.

C. Spatio-Angular Dense Skip Connections

For further enhancing the feature representation extraction process, we propose to improve the information flow with spatio-angular dense skip connections consisting of three types of connections, namely spatial and angular dense skip connections, and image skip connections.

The spatial dense skip connections are intra-correlation-block connections that concatenate the output of shallow spatial convolutional layers to the output of the subsequent layers within a correlation block, i.e., the spatial convolutional layers will receive the features from the preceding layers. Consequently, the spatial convolution function in (4) can be revised as

$$\mathcal{S}(x) = \tilde{\mathcal{C}}_{nS}^S(x) \quad (6)$$

$$\tilde{\mathcal{C}}_i^S(x) = [\mathcal{C}_i^S(\tilde{\mathcal{C}}_{i-1}^S(x)), \tilde{\mathcal{C}}_{i-1}^S(x), \dots, \tilde{\mathcal{C}}_2^S(x), \tilde{\mathcal{C}}_1^S(x)] \quad (7)$$

where $\tilde{\mathcal{C}}_i^S(x)$ represents the i th densely connected spatial convolutional layer and $[\cdot]$ indicates concatenation. The spatial dense skip connections are shown in Figs. 2 and 3 as blue arrows connecting blue tensors under the spatial mode.

The densely connected structure comes with three critical benefits. First, the feature tensors are reinforced with both shallow and deep information, forming hierarchical representations. This is contrary to the previous methods [21] where the shallow features are absent in high-level processing. Second, it facilitates the optimization of the network, especially for the early layers, since every layer will access the gradients directly in backpropagation and the gradient vanish problem is also greatly alleviated. Last but not least, the high trainable parameter utilization leads to model efficiency and prevents overfitting.

While the spatial dense skip connections strengthen the spatial representation within individual correlation blocks,

we explore to bring this benefit to the angular domain by adopting angular dense skip connections that concatenate the output of the preceding correlation blocks F_i to the latter ones. As angular convolutions are connected with their counterparts in the previous correlation blocks, the angular dense skip connections play a role as inter-correlation-block information flow as shown in Fig. 2 as the red arrows.

Furthermore, inspired by the practice of appending raw input to the intermediate layers in video processing [41] and optical flow [56], we introduce image skip connections to provide input X as primitive features for all the blocks. This design is very similar to [41] and [56] as these two methods implicitly estimate the motion between frames and inject raw image information into the intermediate motion feature for further refinement, while in our case, the correlation blocks implicitly model the LF disparity and the raw image offers complementary information for the angular convolutions. The image skip connections are depicted as yellow arrows connecting the input LF and the correlation blocks in Fig. 2.

Accordingly, the function of correlation blocks in (5) are revised into

$$F_i = \begin{cases} [\mathcal{H}(F_{i-1}), F_{i-1}, \dots, F_1, X], & \text{if } i > 1 \\ \mathcal{H}(X), & \text{if } i = 1 \end{cases} \quad (8)$$

where $[\cdot]$ indicates concatenation. The output of the last correlation block $F_{n_{CB}}$ aggregates the feature maps of all the correlation blocks to form hierarchical spatio-angular feature representation. It will be fed to the following SAI reconstruction process.

In [30], the number of feature maps increased by dense skip connections is referred to as the *growth rate*. For simplicity, we keep the growth rates in both domain consistent across the network. Therefore,

$$r_S = r_{CB} = C_1 = C_2$$

where r_S and r_{CB} are growth rates of the spatial and angular dense connections, respectively. Consequently, the number of feature maps of the last correlation block $F_{n_{CB}}$ and the last spatial convolution $\tilde{\mathcal{C}}_{n_S}^S(x)$ in each correlation block will grow to $r_{CB} \times n_{CB}$ and $r_S \times n_S$, respectively. In the experiments of Section IV, the growth rates are set to 32, which are only half of the feature map number used in [21], by virtue of the efficiency of densely connected architecture.

D. SAI Reconstruction

Before reconstruction using the extracted hierarchical correlation features, we follow the practice in [32] to employ a bottleneck layer to aggregate the hierarchical features and reduce the number of the feature maps to 96. Then, the reduced features are reshaped into the angular mode, zero-padded, and fed into an angular convolutional layer with a kernel size of $(U, V, 1, 96, \mathcal{N})$. It shrinks the angular resolution from $(U \times V)$ to (1×1) while producing \mathcal{N} channels, which corresponds to the \mathcal{N} reconstructed SAIs. In Fig. 2, as $(U \times V) = (2 \times 2)$ and $\mathcal{N} = 60$, the kernel size of the angular convolution is $(2, 2, 1, 96, 60)$.

IV. EXPERIMENTS

A. Implementation and Evaluation Details

The proposed SADenseNet is implemented using the deep learning library Keras [58] with Tensorflow [59] backend. The network is trained and tested on a PC with an Intel Core i7-6700K 8-core 4.00 GHz CPU, an Nvidia GTX 1080 Ti GPU, and 32-GB RAM. The source code and trained models are publicly available at <https://huzexi.github.io>.

In regard to training, to conduct a fair comparison, we follow the protocol of [21] to train the network with the training set proposed by Kalantari *et al.* [20], which contains 100 samples. The mini-batch size is set to 2 with a spatial size of (128×128) . The training process is iterated with an Adam optimizer [60] and the learning rate is set to 10^{-4} . We follow the conventional practice to process the luminance channel of the YCbCr color space. The other two channels, namely Cb and Cr, are acquired by upsampling the angular resolution using bicubic interpolation. During training, data augmentation is applied to improve the generalization of the network. We follow the strategies in [25] to randomly flip and rotate the spatial and angular dimensions simultaneously. As a result, the training data can be reused eight times.

n_{CB} and n_S are set to 6 and 5, respectively, as the default values, and the network is trained by minimizing the mean squared error (MSE) loss function as follows:

$$\min_{\hat{Y}} \sum_n \sum_x \sum_y (\hat{Y}(n, x, y) - Y(n, x, y))^2 \quad (9)$$

where n iterates over the reconstructed SAIs and (x, y) indicates a spatial location.

B. Comparison With State-of-the-Art Methods on Real-World Images

First, we compare the SADenseNet's performance on real-world images with the state-of-the-art methods: Kalantari *et al.* [20], HDDRNet [44], NoisyLFRecon [42], and Yeung *et al.* [21].

Experiments are conducted on four real-world LF datasets, namely 30 Scenes [20], EPFL [61], Occlusions [62], and Reflective [62] that are captured by Lytro Illum cameras [18]. These four datasets contain 30, 118, 43, and 31 LF images. The LF images that have appeared in the 100-sample training set are removed for fairness. In each LF image, the angular resolution is (14×14) and the spatial resolution is (376×541) . During the evaluation, only the central (8×8) SAIs are adopted as the rest are dark and noisy, and 22 pixels of the four borders in the spatial resolution are also shaved as in [20]. The reconstruction is performed from (2×2) SAIs to (8×8) SAIs. The reconstruction quality is measured by PSNR and structural similarity index (SSIM) in RGB color space.

The results are shown in Table I. It can be observed that SADenseNet has outperformed the other methods observably. Compared with the best of them, in [21], SADenseNet outperforms by more than 1.00 dB PSNR in all datasets except the Reflective dataset where our proposed approach has a reconstruction advantage of 0.71 dB PSNR.

TABLE I

OVERALL COMPARISON WITH THE STATE OF THE ART ON THE REAL-WORLD DATASETS. THE TABLE IS DIVIDED INTO TWO PARTS. FIRST, THE SECOND-TO-FOURTH COLUMNS ARE PSNR AND SSIM ON FOUR DATASETS. THE NUMBER OF IMAGE SAMPLES IN A PARTICULAR DATASET IS SHOWN IN PARENTHESES. SECOND, THE LAST TWO COLUMNS DISPLAY THE NUMBER OF PARAMETERS AND RUNNING SPEED. BOLD SCORES INDICATE THE BEST RESULTS. THE LAST ROW IS THE DIFFERENCES BETWEEN SADENSENET AND YEUNG *et al.* [21]

Method	30 Scenes (30)	EPFL (118)	Occlusions (43)	Reflective (31)	# Parameters	Speed/s
Kalantari <i>et al.</i> [20]	38.31/0.9755	38.76/0.9586	31.82/0.8973	35.91/0.9415	1,644,204	721.05
HDDRNet [44]	37.52/0.9664	38.58/0.9547	32.36/0.9071	36.32/0.9443	16,558,848	1434.65
NoisyLFRecon [42]	38.90/0.9776	39.01/0.9639	32.12/0.9070	36.36/0.9455	20,277,551	32.92
Yeung <i>et al.</i> [21]	39.16/0.9782	39.53/0.9641	32.66/0.9073	36.44/0.9458	1,498,752	38.05
SADenseNet(Ours)	40.31/0.9836	40.54/0.9706	33.76/0.9269	37.15/0.9521	1,134,140	12.82
Difference	+1.15/+0.0054	+1.01/+0.0065	+1.10/+0.0196	+0.71/+0.0063	75.67%	$\approx 3 \times$ faster

TABLE II

PERFORMANCE COMPARISON WITH THE STATE OF THE ART ON THE SYNTHETIC HCI DATASET [57]. PSNR AND SSIM ARE GIVEN. BOLD SCORES INDICATE THE BEST RESULTS. THE DIFFERENCES BETWEEN SADENSENET AND YEUNG *et al.* [21] ARE PRESENTED IN THE LAST ROW

Method	Buddha	Mona	Average
Kalantari <i>et al.</i> [20]	42.73/0.9844	42.42/0.9858	42.58/0.9851
Wu <i>et al.</i> [24]	43.20/0.9963	44.37/0.9977	43.79/0.9981
Yeung <i>et al.</i> [21]	43.77/0.9872	45.67/0.9920	44.72/0.9896
SADenseNet(Ours)	45.82/0.9921	46.84/0.9932	46.33/0.9927
Difference	+2.05/+0.0049	+1.17/+0.0012	+1.61/+0.0031

For a better understanding of the performance gains, selected visual results from the four test datasets are presented in Fig. 4. It is visible that our error maps are basically clearer than the other prior arts. Concretely, the reconstructed edges of the objects are more complete in *IMG_1528*, e.g., the lamp pole behind the leaves in the red bounding box and the sign above the vehicles in the blue bounding box. The lamp pole example poses a major challenge to LF reconstruction as it is occluded by the leaves in some SAIs. Such a phenomenon can also be observed at the fence border in the red bounding box of *Occlusions_29* and the English letter behind the leaves in the blue bounding box of *Reflective_12*. This can be attributed to the abundant spatio-angular representation in handling the appearance that is visible in limited SAIs. Similar improvement can also be observed in the reconstruction of complicated details, e.g., the flower cores in the blue and red boxes of *Mirabelle_Pruné_Tree*, and the windows in the blue bounding box of *Occlusions_29*, which are entirely blurred in the result of most methods. In *Reflective_12*, it is very obvious that the method of HDDRNet [44] and Yeung *et al.* [21] incorrectly reconstructs a large area of shadow at the bottom left corner, while SADenseNet successfully reconstructs it with the long-term information supplied by the dense skip connections [31] and enlarged spatial receptive fields of the correlation blocks and HDDRNet [44] and Yeung *et al.* [21] confined the correlation information and falsely rendered the shadow across all SAIs.

On the other hand, to demonstrate the model's efficiency, we compare the memory cost in terms of the number of trainable parameters and the computation cost in terms of the testing speed, as reported in Table I. The speed tests are operated

in CPU-only mode. The results demonstrate that the method of Kalantari *et al.* [20] and NoisyLFRecon [42] is plagued by their explicit disparity estimation and warping process. Also, their SAI synthesis functions must be performed separately for each SAI as the intermediate information cannot be shared ending up with a very low processing speed. Regarding the memory cost, HDDRNet [44] and NoisyLFRecon [42] employ a relatively huge model as the former hires 4-D convolution operators and the latter adopts a modified ResNet-50, which has taken more than 19 million parameters. These two means aim at extracting an expressive feature representation but lead to a huge model instead of improvement in reconstruction performance. On the other hand, the end-to-end separable-convolution-based methods, [21] and SADenseNet, reconstruct SAIs in one propagation at a substantially faster speed. Moreover, compared with [21], our SADenseNet requires only 3/4 of parameters and is nearly three times faster. The achievement can be attributed to the correlation blocks with efficient convolutions and spatio-angular dense skip connections that improve information flow.

C. Comparison With State-of-the-Art Methods on Synthetic Images

The performance of SADenseNet is also evaluated on the synthetic HCI dataset [57]. We follow the practice of Wu *et al.* [24] and Yeung *et al.* [21] to calculate PSNR and SSIM on the Y channel only over the (3×3) to (9×9) reconstruction task. The results on *Buddha* and *Mona* are reported in Table II. SADenseNet has produced competitive results exceeding Yeung *et al.* [21] by 1.61 dB PSNR averagely. In regard to SSIM, SADenseNet has obtained the closest results to the ones reported by Wu *et al.* in [24] while outperforming its PSNR significantly likewise.

The reconstruction quality of the two testing images has been visualized in Fig. 5. The most significant difference in *Buddha* is located at the edges of the bricks on the floor where SADenseNet does not produce the blurring artifacts as [21]. Similar improvement has been observed in *Mona* where artifacts are produced around the leaf border in [21] but not seen in SADenseNet.

D. Ablation Studies

To further study the nature of SADenseNet, a series of ablation studies are conducted in this section. We keep the



Fig. 4. Visualization of the reconstruction quality of the selected real-world scenes. The angular locations are indicated at the top-left corner in the ground truth. In each sample, the first row is pixel-wise error visualized as heat maps in the first row, the second row is zoomed-in views of the selected regions in the red and blue boxes, and the third row is the sample title and PSNR/SSIM.

TABLE III

COMPARISON OF PERFORMANCE WITH DIFFERENT n_S .
THE BASELINE VARIANT IS UNDERLINED

n_S	30 Scenes	# Parameters	Speed/s
6	40.34/0.9839	1,466,108	16.25
<u>5</u>	40.31/0.9836	1,134,140	12.82
4	40.15/0.9831	857,468	9.96
3	40.01/0.9824	636,092	7.30
2	39.80/0.9815	470,012	5.72
1	38.28/0.9787	359,228	4.18

TABLE IV

COMPARISON OF PERFORMANCE WITH DIFFERENT n_A .
THE BASELINE VARIANT IS UNDERLINED

n_A	30 Scenes	# Parameters	Speed/s
1	40.31/0.9836	1,134,140	12.82
<u>2</u>	40.27/0.9834	1,189,628	13.48
3	40.19/0.9834	1,245,116	14.26

previous configuration in Section IV-B to conduct the studies on real-world datasets.

1) *Spatio-Angular Dense Skip Connections*: In Section III-C, we have introduced three kinds of dense skip

connections to enhance the information flow. To discover the contribution of these connections, we create several variants with or without them. For simplicity, spatial, angular, and image connections are denoted as S , A , and I , respectively. Eight variants, each processed a unique combination of connections, are reported in Table VI. SADenseNet_ISA

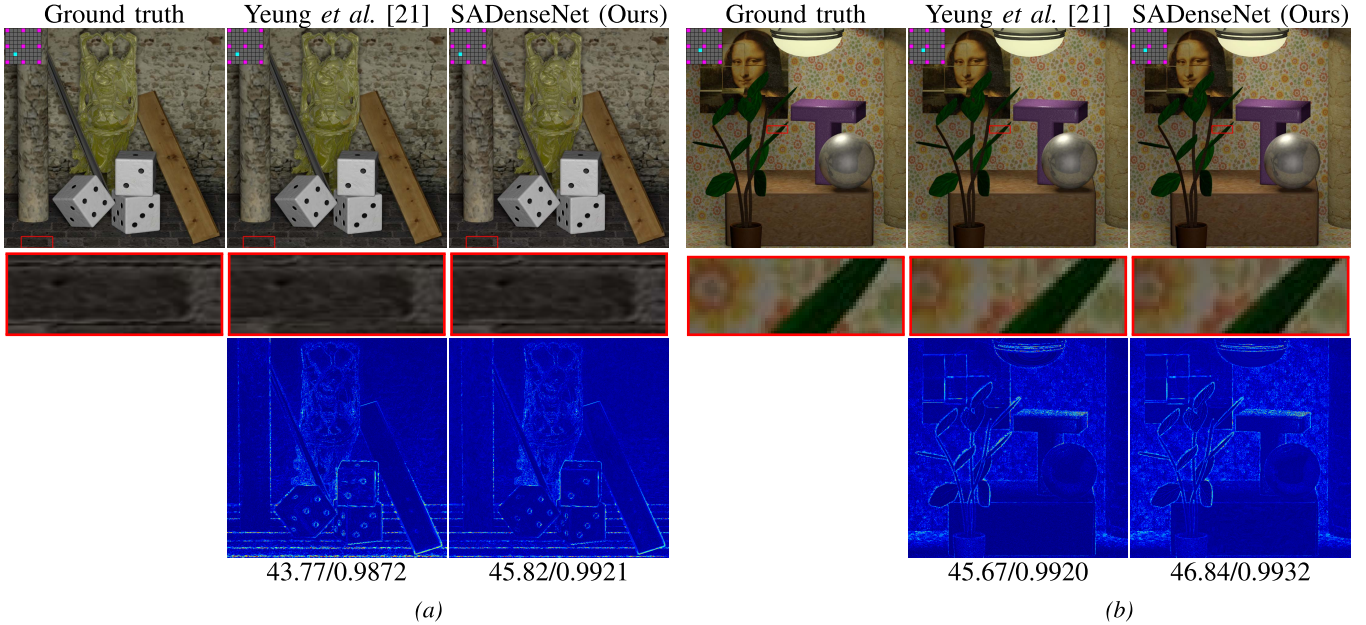


Fig. 5. Visualization of reconstruction quality of the selected scenes in the synthetic HCI dataset [57]. (a) *Buddha* and (b) *Mona*. In each sample, the three columns correspond to ground truth, and the results of Yeung *et al.* [21] and SADenseNet. Zoomed-in views of selected regions in the first row are displayed in the red boxes of the second row. Error maps are depicted as heat maps in the third row.

TABLE V
COMPARISON OF PERFORMANCE WITH DIFFERENT n_{CB} .
THE BASELINE VARIANT IS UNDERLINED

n_{CB}	30 Scenes	# Parameters	Speed/s
7	40.31/0.9835	1,346,588	14.98
<u>6</u>	40.31/0.9836	<u>1,134,140</u>	12.82
5	40.21/0.9834	930,908	10.52
4	40.03/0.9824	736,892	8.36
3	39.91/0.9819	552,092	6.48
2	39.61/0.9804	376,508	4.30
1	38.35/0.9735	210,240	2.41

is effectively the full version of SADenseNet. n_{CB} and n_S remain 6 and 5, respectively, for all the variants. In Table VI, it is obvious that reconstruction quality deteriorates if any connection is removed. For a better understand of the connections, we visualize the training process of the variants in Fig. 6, and their performance against model sizes and speed in Fig. 7. We set the full version, SADenseNet_ISA, as the baseline in this study, and the results of the prior arts, Kalantari *et al.* [20] and Yeung *et al.* [21], are also plotted.

In terms of reconstruction quality, while all types of connections outperform SADenseNet_None significantly, the biggest performance gain is achieved by the angular connections as SADenseNet_A surpasses SADenseNet_S and SADenseNet_I by 0.32 and 0.14 dB in 30 Scenes, respectively.

It is observed that the three kinds of dense skip connections are complementary as combining any two or three of them leads to further performance gains. Besides, all variants have outperformed the prior arts by at least 0.40 dB PSNR except SADenseNet_None, which is without any skip connections inducing drastic decline, proving the importance of the three kinds of skip connections.

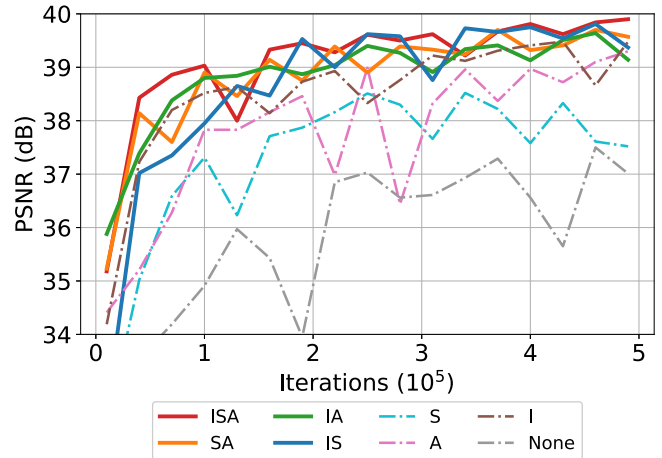


Fig. 6. Training process of SADenseNet variants. The first 5×10^5 iterations are plotted. The variants with multiple connections are indicated by solid lines while the ones with a single connection or none are indicated by dashed lines. For visual effect, some curves are partially truncated.

In Fig. 7(a) and (b), in terms of the x -axis, it is observed that all the SADenseNet variants have fewer parameters and higher speeds. While the prior arts take 32.92 s in [42], 38.05 s in [21], and even more than 700 s in [20] and [44] to reconstruct a full LF image, SADenseNet variants take less than half of the time. It is worth noticing that while SADenseNet_ISA has achieved the best reconstruction quality with a large model size similar to Yeung *et al.* [21], the suboptimal variant SADenseNet_IA is capable of achieving approximate performance, 40.18 dB PSNR, 0.13 dB lower than SADenseNet_ISA, but it uses only 0.58 million parameters, which is about half of SADenseNet_ISA, manifesting to be an

TABLE VI

PERFORMANCE COMPARISON OF SADENSENET VARIANTS ON REAL-WORLD DATASETS. THE TABLE IS DIVIDED INTO THREE PARTS: 1) THE SECOND-TO-FOURTH COLUMNS ARE THE PROPERTIES OF THE VARIANTS; 2) THE FIFTH-TO-EIGHTH COLUMNS ARE PSNR AND SSIM EVALUATED ON FOUR DATASETS; AND 3) THE LAST TWO COLUMNS DISPLAY THE NUMBER OF PARAMETERS AND RUNNING SPEED. THE BASELINE VARIANT IS UNDERLINED

Name	Spatial	Angular	Image	30 Scenes (30)	EPFL (118)	Occlusions (43)	Reflective (31)	# Parameters	Speed/s
SADenseNet_None				38.76/0.9776	39.25/0.9642	32.63/0.9123	36.25/0.9453	394,844	4.9
SADenseNet_I			✓	39.85/0.9818	40.17/0.9683	33.30/0.9221	36.90/0.9494	396,860	5.17
SADenseNet_S	✓			39.67/0.9815	39.89/0.9678	33.19/0.9199	36.79/0.9492	947,804	11.15
SADenseNet_A		✓		39.99/0.9822	40.21/0.9686	33.40/0.9207	36.99/0.9495	579,164	6.35
SADenseNet_SA	✓	✓		40.10/0.9828	40.30/0.9692	33.49/0.9241	37.08/0.9496	1,132,124	12.31
SADenseNet_IA		✓	✓	40.18/0.9831	40.42/0.9701	33.67/0.9274	37.06/0.9507	581,180	6.42
SADenseNet_IS	✓		✓	40.14/0.9832	40.32/0.9699	33.53/0.9238	37.05/0.9500	949,820	11.79
SADenseNet_ISA	✓	✓	✓	40.31/0.9836	40.54/0.9706	33.76/0.9267	37.15/0.9521	1,134,140	12.82

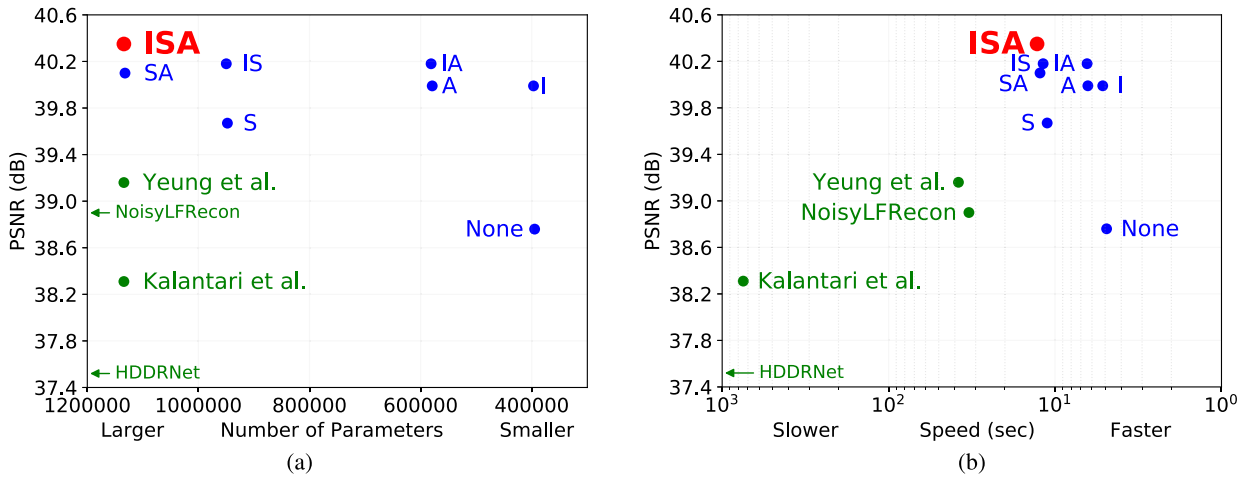


Fig. 7. Plots of the tradeoff between reconstruction quality and costs of the SADenseNet variants and rivals. PSNR evaluated on 30 Scenes [20] is depicted as the metric of performance. The variants are in blue, while the baseline SADenseNet_ISA is in red. The compared methods are in green. For simplicity, the variants' prefix is omitted, and some items are indicated with arrows instead of dots as they are out of the scope. Generally, items in the top-right corners can handle the tradeoff better with better performance and at smaller costs simultaneously. (a) PSNR versus numbers of parameters. (b) PSNR versus speed.

economic option under a tight memory constraint. The speed of SADenseNet_IA is about $2 \times$ faster than the variants with spatial connections as it gets rid of the relatively costly spatial connections. Meanwhile, SADenseNet_I is also a considerable choice to pursue a lightweight model under a tighter condition, which takes a similar number of parameters and running speed with SADenseNet_None but achieves 39.85 dB PSNR, 1.09 dB higher.

Regarding the training process plotted in Fig. 6, the curves demonstrate how these connections improve the information flow and benefit the convergence of the network during training. For simplicity, we only plot the first 5×10^5 iterations with PSNR. The curves appear more stable when multiple connections are used, i.e., SADenseNet_ISA, SADenseNet_SA, SADenseNet_IA, and SADenseNet_IS, while the ones with either spatial connections, angular connections, or none have encountered sudden drops in PSNR. We deduce that the improvement of training stability is derived from the combination of spatial and angular dense connected information flow. However, SADenseNet_I is the only exception having a stable curve, suggesting that this type of connection is complementary to the extracted spatio-angular features while training. This impact is also verified by comparing SADenseNet_IA and SADenseNet_IS with SADenseNet_A and SADenseNet_S.

It is also witnessed that SADenseNet_ISA, trained with 1.5×10^5 iterations in around 14 h, has already outperformed the best result of Yeung *et al.* [21], which requires ten days of training on a similar GPU.

With the analysis from the test scenario and the training process, we can draw a conclusion that the proposed three kinds of dense skip connections can enhance the information flow of SADenseNet to facilitate a quick and stable convergence when training and improve the reconstruction performance, while the model remains efficient in computation and memory usage.

2) *Domain Asymmetry*: As described in Section I, we hypothesize the domain asymmetry in the spatial and angular domains. In this section, we validate this hypothesis by evaluating the performance with different n_S values on 30 Scenes [20] dataset. The number of correlation blocks n_{CB} is fixed to 6 and we set $n_S = 5$ as the baseline. As shown in Table III, the performance reduces gradually as n_S decreases. It is worth noticing that when n_S decreases to 1, a correlation block virtually degrades to an SAS convolution as in [21], which achieves the worst results of 38.28 dB, declining by 2.03 dB, suggesting that it hampers the performance by treating the two domains symmetrically. Moreover, when adding more spatial convolutions to the baseline, the

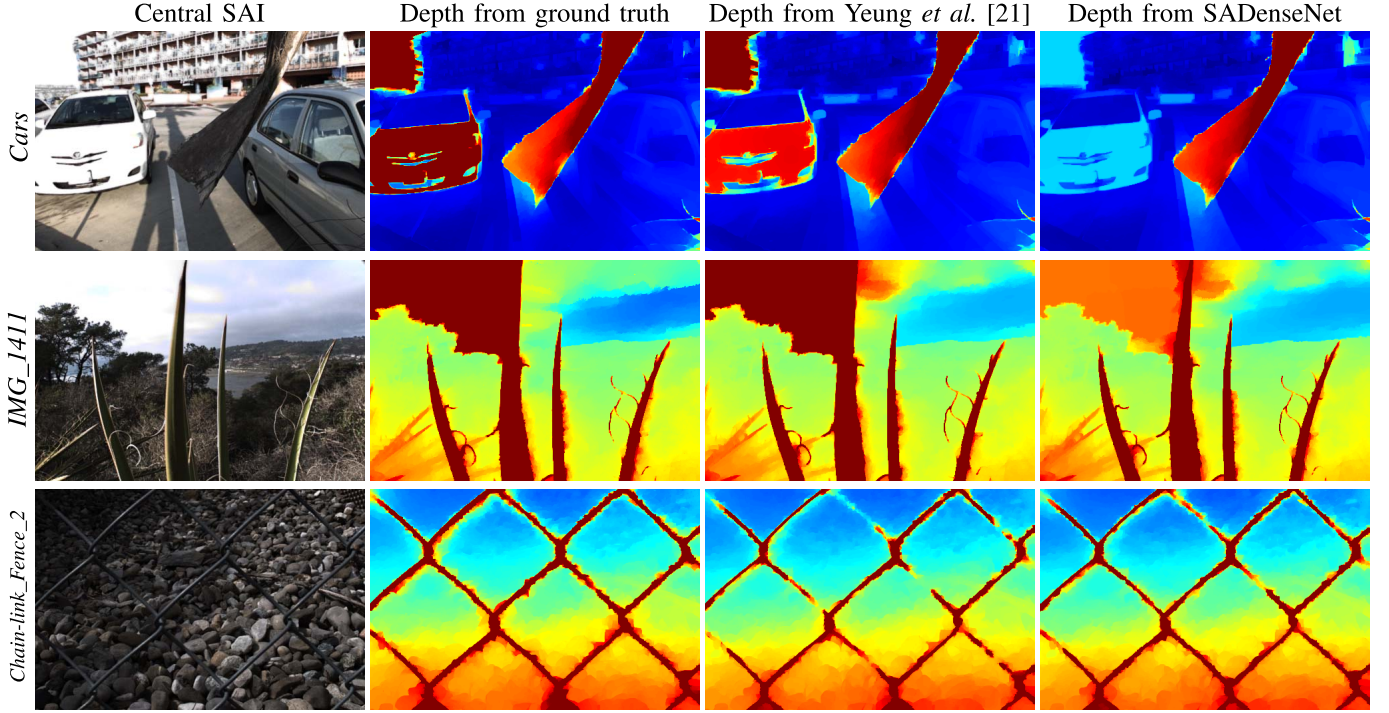


Fig. 8. Estimated depth of selected examples. The first column is the raw image information followed by three columns with depth maps estimated by the method of Chen *et al.* [13] on the full LF of the ground truth, the reconstructed LF of Yeung *et al.* [21], and SADenseNet.

performance gain is marginal. When $n_S = 6$, PSNR increases by merely 0.03 dB, but 29% more parameters and about 22% lower speed are incurred. This suggests that the influence of deeper spatial features has saturated.

On the other hand, we modify the correlation blocks to append more angular convolutions. The number of angular convolutions in each block is denoted as n_A , and the other variables n_{CB} and n_S are fixed to 6 and 5, respectively. In each block, only the last angular convolution is densely connected with other blocks. Such a modification seems likely to obtain deeper angular features; however, the results in Table IV disagree with the speculation. Harmful effects are recorded that when $n_A = 2$ and 3, the PSNR declines by 0.04 and 0.12 dB compared with the baseline, let alone the incurred computation and memory cost, proving that employing more angular convolutions is in vain.

Given the results on n_S and n_A , we can conclude that domain asymmetry exists in LF data, and the correlation blocks are proved effective to extract spatio-angular features with asymmetrical operations.

3) Correlation Blocks: To verify the effectiveness of stacking correlation blocks, we evaluate the performance by varying the number of blocks n_{CB} . As demonstrated in Table V, the performance is rising as n_{CB} increases and reaches the highest point at $n_{CB} = 6$, which is used as the baseline. When n_{CB} increases to 7, the performance slightly drops, which suggests that the performance gain brought by a deeper architecture has been saturated, and adding more correlation blocks will lead to deterioration.

Remarkably, the $n_{CB} = 2$ variant has outperformed Yeung *et al.* [21] by 0.45 dB PSNR with only 33% parameters and $8.8\times$ faster speed, another convincing proof of the

architecture's effectiveness and another option to obtain a lightweight but powerful model by employing fewer correlation blocks.

E. Depth Estimation

Depth estimation is one of the important LF measurement applications. As SAIs are reconstructed, we further investigate the depth maps estimated from the densely sampled LF to demonstrate SADenseNet's reconstruction quality from another perspective. Fig. 8 gives some selected images' depth maps generated from the ground truth, the densely sampled LF reconstructed by Yeung *et al.* [21], and SADenseNet using the estimation method of [13]. It can be observed that SADenseNet has produced visibly better depth maps than Yeung *et al.* [21] with high-quality object edges in *Chain-link_Fence_2*. It is interesting that in *Cars* and *IMG_1411*, depth generated on SADenseNet's reconstructed SAIs is more satisfactory than ground truth. In *Cars*, the car on the left should be located between the metal plate in the foreground and the building in the background. Both ground truth and Yeung *et al.* [21] misclassify it as having a similar depth to the metal plate. The misclassification mainly happens in textureless areas such as the sky in the top-left corner of *Cars* and to the left of the plant in *IMG_1411*. However, depth maps estimated with SADenseNet do not suffer from this problem.

The depth predictions in Fig. 8 suggest that the region of the textureless areas and the foreground objects becomes more distinguishable to the depth estimation algorithm [13] after being preprocessed by our proposed method. One plausible explanation for such improvement is that the prior learned by our proposed method is able to refine the input LF during reconstruction before feeding into the depth estimation

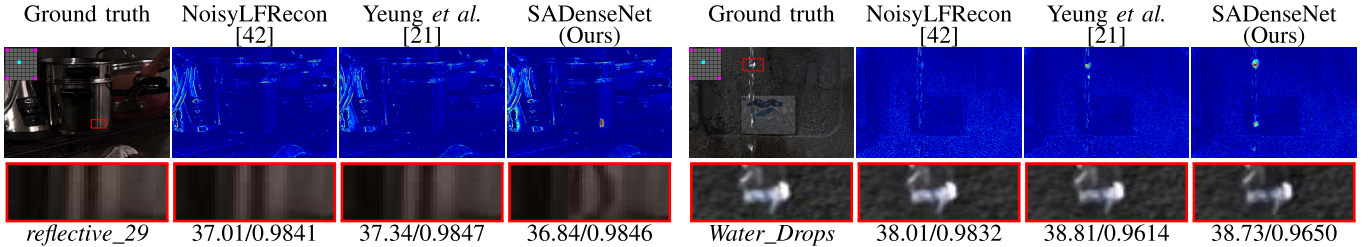


Fig. 9. Visualization of failed examples of SADenseNet. Error maps are depicted as heat maps in the first row, zoomed-in views of selected regions are displayed in the red boxes in the second row, and sample titles and PSNR/SSIM are given in the last row.

algorithm. In conclusion, SADenseNet not only produces high reconstruction quality but also supplies complementary information to improve the accuracy of depth estimation and other measurement applications.

F. Limitations

Even though SADenseNet has demonstrated superior performance in the task of LF reconstruction, it does not necessarily outperform other methods across all samples. While there are 222 real-world samples tested in the previous evaluation, SADenseNet fails 14 of them, in most of which reflective surfaces are presented. Two of them are visualized in Fig. 9 with NoisyLFRecon [42] and Yeung *et al.* [21] as the representatives of disparity- and separable-convolution-based methods, respectively.

In *reflective_29*, it is observed that SADenseNet is outperformed by Yeung *et al.* [21] by 0.5 dB PSNR, and in the error maps, the reflective surface of the steel pot is reconstructed with distorted artifacts in the red box, which does not happen in the results of the other two methods. In the other example, *Water_Drops*, in spite of the higher PSNR and SSIM achieved by Yeung *et al.* [21] and SADenseNet, the flaw can be easily spotted in their error maps that the reflective water drops are not correctly reconstructed, while NoisyLFRecon [42] is not confused by these reflections with a visibly clearer error map. Given these results, we presumed that disparity-based methods are more robust to the scenes with reflective surfaces, which remains a problem for our method to study in future research.

V. CONCLUSION

In this article, we have studied domain asymmetry in LF images and proposed correlation blocks to extract spatio-angular feature representation in an asymmetrical manner. For further enhancing the spatio-angular representation, we have applied spatial and angular dense skip connections to construct a compact information flow. Moreover, additional image skip connections are utilized to complement the correlation features with raw image information, forming our final SADenseNet. Experiments on four real-world datasets and a synthetic dataset have demonstrated its state-of-the-art performance at significantly lower costs. Ablation studies have verified the benefits of the skip connections and the efficacy of the proposed asymmetrical processing in the spatial and angular domains using the correlation blocks. Furthermore, we have found that some lightweight variants of our proposed method, i.e., the model

without spatial dense skip connections or that employing only two correlation blocks, can still achieve impressive performance with very few resources when there are some constrained conditions. Finally, we have performed depth estimation as a typical LF measurement task on the reconstructed LF images, and the result has proved SADenseNet's promising potential of improving LF-related measurement performance.

REFERENCES

- [1] R. Raghavendra, K. B. Raja, and C. Busch, "Presentation attack detection for face recognition using light field camera," *IEEE Trans. Image Process.*, vol. 24, no. 3, pp. 1060–1075, Mar. 2015.
- [2] Z. Ji, H. Zhu, and Q. Wang, "LFHOG: A discriminative descriptor for live face detection from light field image," in *Proc. IEEE Int. Conf. Image Process. (ICIP)*, Sep. 2016, pp. 1474–1478.
- [3] H. Sellahewa and S. A. Jassim, "Image-quality-based adaptive face recognition," *IEEE Trans. Instrum. Meas.*, vol. 59, no. 4, pp. 805–813, Apr. 2010.
- [4] L. Fang and S. Li, "Face recognition by exploiting local Gabor features with multitask adaptive sparse representation," *IEEE Trans. Instrum. Meas.*, vol. 64, no. 10, pp. 2605–2615, Oct. 2015.
- [5] T.-C. Wang, J.-Y. Zhu, E. Hiroaki, M. Chandraker, A. A. Efros, and R. Ramamoorthi, "A 4D light-field dataset and CNN architectures for material recognition," in *Computer Vision—ECCV 2016*. Cham, Switzerland: Springer, 2016, pp. 121–138. [Online]. Available: https://link.springer.com/chapter/10.1007/978-3-319-46487-9_8
- [6] Z. Lu, H. W. F. Yeung, Q. Qu, Y. Y. Chung, X. Chen, and Z. Chen, "Improved image classification with 4D light-field and interleaved convolutional neural network," *Multimedia Tools Appl.*, vol. 78, no. 20, pp. 29211–29227, Oct. 2019.
- [7] G. Song, K. Song, and Y. Yan, "EDRNet: Encoder-decoder residual network for salient object detection of strip steel surface defects," *IEEE Trans. Instrum. Meas.*, vol. 69, no. 12, pp. 9709–9719, Dec. 2020.
- [8] H. Sheng, S. Zhang, X. Liu, and Z. Xiong, "Relative location for light field saliency detection," in *Proc. IEEE Int. Conf. Acoust., Speech Signal Process. (ICASSP)*, Mar. 2016, pp. 1631–1635.
- [9] M. Zhang *et al.*, "LFNet: Light field fusion network for salient object detection," *IEEE Trans. Image Process.*, vol. 29, pp. 6276–6287, 2020.
- [10] S. Heber, W. Yu, and T. Pock, "Neural EPI-volume networks for shape from light field," in *Proc. IEEE Int. Conf. Comput. Vis. (ICCV)*, Oct. 2017, pp. 2271–2279.
- [11] H.-G. Jeon *et al.*, "Depth from a light field image with learning-based matching costs," *IEEE Trans. Pattern Anal. Mach. Intell.*, vol. 41, no. 2, pp. 297–310, Feb. 2019.
- [12] T.-C. Wang, A. A. Efros, and R. Ramamoorthi, "Occlusion-aware depth estimation using light-field cameras," in *Proc. IEEE Int. Conf. Comput. Vis. (ICCV)*, Dec. 2015, pp. 3487–3495.
- [13] J. Chen, J. Hou, Y. Ni, and L.-P. Chau, "Accurate light field depth estimation with superpixel regularization over partially occluded regions," *IEEE Trans. Image Process.*, vol. 27, no. 10, pp. 4889–4900, Oct. 2018.
- [14] H.-Y. Lin, C.-L. Tsai, and V. L. Tran, "Depth measurement based on stereo vision with integrated camera rotation," *IEEE Trans. Instrum. Meas.*, vol. 70, pp. 1–10, 2021.

- [15] E. Lilienblum and A. Al-Hamadi, "A structured light approach for 3-D surface reconstruction with a stereo line-scan system," *IEEE Trans. Instrum. Meas.*, vol. 64, no. 5, pp. 1258–1266, May 2015.
- [16] *Raytrix 3D Light Field Camera Technology*. Accessed: Oct. 22, 2018. [Online]. Available: <https://raytrix.de/>
- [17] C. Heinze, S. Spyropoulos, S. Hussmann, and C. Perwass, "Automated robust metric calibration algorithm for multifocus plenoptic cameras," *IEEE Trans. Instrum. Meas.*, vol. 65, no. 5, pp. 1197–1205, May 2016.
- [18] *Lytro*. Accessed: Oct. 22, 2018. [Online]. Available: <https://www.lytro.com/>
- [19] Z. Niu, X. Zhang, J. Ye, L. Ye, R. Zhu, and X. Jiang, "Adaptive phase correction for phase measuring deflectometry based on light field modulation," *IEEE Trans. Instrum. Meas.*, vol. 70, pp. 1–10, 2021.
- [20] N. K. Kalantari, T.-C. Wang, and R. Ramamoorthi, "Learning-based view synthesis for light field cameras," *ACM Trans. Graph.*, vol. 35, no. 6, p. 193, 2016.
- [21] H. W. F. Yeung, J. Hou, J. Chen, Y. Y. Chung, and X. Chen, "Fast light field reconstruction with deep coarse-to-fine modeling of spatial-angular clues," in *Proc. Eur. Conf. Comput. Vis. (ECCV)*, Sep. 2018, pp. 137–152.
- [22] G. Wu, M. Zhao, L. Wang, Q. Dai, T. Chai, and Y. Liu, "Light field reconstruction using deep convolutional network on EPI," in *Proc. IEEE Conf. Comput. Vis. Pattern Recognit. (CVPR)*, Jul. 2017, p. 2.
- [23] H. W. F. Yeung, J. Hou, X. Chen, J. Chen, Z. Chen, and Y. Y. Chung, "Light field spatial super-resolution using deep efficient spatial-angular separable convolution," *IEEE Trans. Image Process.*, vol. 28, no. 5, pp. 2319–2330, May 2019.
- [24] G. Wu, Y. Liu, L. Fang, Q. Dai, and T. Chai, "Light field reconstruction using convolutional network on EPI and extended applications," *IEEE Trans. Pattern Anal. Mach. Intell.*, vol. 41, no. 7, pp. 1681–1694, Jul. 2019.
- [25] C. Shin, H.-G. Jeon, Y. Yoon, I. S. Kweon, and S. J. Kim, "EPINET: A fully-convolutional neural network using epipolar geometry for depth from light field images," in *Proc. IEEE/CVF Conf. Comput. Vis. Pattern Recognit.*, Jun. 2018, pp. 4748–4757.
- [26] S. Heber, W. Yu, and T. Pock, "U-shaped networks for shape from light field," in *Proc. Brit. Mach. Vis. Conf.*, vol. 1, 2016, pp. 37.1–37.12.
- [27] Y. Wang, F. Liu, Z. Wang, G. Hou, Z. Sun, and T. Tan, "End-to-end view synthesis for light field imaging with pseudo 4DCNN," in *Proc. Eur. Conf. Comput. Vis. (ECCV)*, Sep. 2018, pp. 333–348.
- [28] K. Simonyan and A. Zisserman, "Very deep convolutional networks for large-scale image recognition," in *Proc. Int. Conf. Learn. Represent. (ICRL)*, 2015, pp. 1–14.
- [29] J. Kim, J. K. Lee, and K. M. Lee, "Accurate image super-resolution using very deep convolutional networks," in *Proc. IEEE Conf. Comput. Vis. Pattern Recognit. (CVPR)*, Jun. 2016, pp. 1646–1654.
- [30] G. Huang, Z. Liu, L. Van Der Maaten, and K. Q. Weinberger, "Densely connected convolutional networks," in *Proc. IEEE Conf. Comput. Vis. Pattern Recognit. (CVPR)*, Jul. 2017, pp. 4700–4708.
- [31] Y. Tai, J. Yang, X. Liu, and C. Xu, "MemNet: A persistent memory network for image restoration," in *Proc. IEEE Int. Conf. Comput. Vis. (ICCV)*, Oct. 2017, pp. 4539–4547.
- [32] T. Tong, G. Li, X. Liu, and Q. Gao, "Image super-resolution using dense skip connections," in *Proc. IEEE Int. Conf. Comput. Vis. (ICCV)*, Oct. 2017, pp. 4809–4817.
- [33] M. Haris, G. Shakhnarovich, and N. Ukita, "Deep back-projection networks for super-resolution," in *Proc. IEEE/CVF Conf. Comput. Vis. Pattern Recognit.*, Jun. 2018, pp. 1664–1673.
- [34] Z. Li, J. Yang, Z. Liu, X. Yang, G. Jeon, and W. Wu, "Feedback network for image super-resolution," in *Proc. IEEE/CVF Conf. Comput. Vis. Pattern Recognit. (CVPR)*, Jun. 2019, pp. 3867–3876.
- [35] S. Pujades, F. Devernay, and B. Goldluecke, "Bayesian view synthesis and image-based rendering principles," in *Proc. IEEE Conf. Comput. Vis. Pattern Recognit.*, Jun. 2014, pp. 3906–3913.
- [36] Z. Zhang, Y. Liu, and Q. Dai, "Light field from micro-baseline image pair," in *Proc. IEEE Conf. Comput. Vis. Pattern Recognit. (CVPR)*, Jun. 2015, pp. 3800–3809.
- [37] S. Wanner and B. Goldluecke, "Variational light field analysis for disparity estimation and super-resolution," *IEEE Trans. Pattern Anal. Mach. Intell.*, vol. 36, no. 3, pp. 606–619, Mar. 2014.
- [38] E. Penner and L. Zhang, "Soft 3D reconstruction for view synthesis," *ACM Trans. Graph.*, vol. 36, no. 6, pp. 235:1–235:11, 2017.
- [39] H. Zheng, M. Ji, H. Wang, Y. Liu, and L. Fang, "CrossNet: An end-to-end reference-based super resolution network using cross-scale warping," in *Proc. Eur. Conf. Comput. Vis. (ECCV)*, 2018, pp. 88–104.
- [40] C. Peng, X. Zhang, G. Yu, G. Luo, and J. Sun, "Large kernel matters—Improve semantic segmentation by global convolutional network," in *Proc. IEEE Conf. Comput. Vis. Pattern Recognit. (CVPR)*, Jul. 2017, pp. 1743–1751.
- [41] J. Caballero *et al.*, "Real-time video super-resolution with spatio-temporal networks and motion compensation," in *Proc. IEEE Conf. Comput. Vis. Pattern Recognit.*, Jul. 2017, pp. 4778–4787.
- [42] W. Zhou, J. Shi, Y. Hong, L. Lin, and E. E. Kuruoglu, "Robust dense light field reconstruction from sparse noisy sampling," *Signal Process.*, vol. 186, Sep. 2021, Art. no. 108121.
- [43] C. Szegedy *et al.*, "Going deeper with convolutions," in *Proc. IEEE Conf. Comput. Vis. Pattern Recognit. (CVPR)*, Jun. 2015, pp. 1–9.
- [44] N. Meng, H. K.-H. So, X. Sun, and E. Y. Lam, "High-dimensional dense residual convolutional neural network for light field reconstruction," *IEEE Trans. Pattern Anal. Mach. Intell.*, vol. 43, no. 3, pp. 873–886, Mar. 2021.
- [45] P. Chandramouli, K. V. Gandikota, A. Gorlitz, A. Kolb, and M. Moeller, "A generative model for generic light field reconstruction," *IEEE Trans. Pattern Anal. Mach. Intell.*, early access, Nov. 23, 2020, doi: [10.1109/TPAMI.2020.303941](https://doi.org/10.1109/TPAMI.2020.303941).
- [46] M. Guo, J. Hou, J. Jin, J. Chen, and L.-P. Chau, "Deep spatial-angular regularization for compressive light field reconstruction over coded apertures," in *Computer Vision—ECCV 2020*. Cham, Switzerland: Springer, 2020, pp. 278–294. [Online]. Available: https://link.springer.com/chapter/10.1007/978-3-030-58536-5_17
- [47] Y. Inagaki, Y. Kobayashi, K. Takahashi, T. Fujii, and H. Nagahara, "Learning to capture light fields through a coded aperture camera," in *Proc. Eur. Conf. Comput. Vis. (ECCV)*, 2018, pp. 418–434.
- [48] K. He, X. Zhang, S. Ren, and J. Sun, "Deep residual learning for image recognition," in *Proc. IEEE Conf. Comput. Vis. Pattern Recognit. (CVPR)*, Jun. 2016, pp. 770–778.
- [49] Y. Tai, J. Yang, and X. Liu, "Image super-resolution via deep recursive residual network," in *Proc. IEEE Conf. Comput. Vis. Pattern Recognit. (CVPR)*, Jul. 2017, pp. 3147–3155.
- [50] Y. Zhang, K. Li, K. Li, L. Wang, B. Zhong, and Y. Fu, "Image super-resolution using very deep residual channel attention networks," in *Proc. Eur. Conf. Comput. Vis.*, 2018, pp. 286–301.
- [51] Y. Song, C. Ma, L. Gong, J. Zhang, R. W. H. Lau, and M.-H. Yang, "CREST: Convolutional residual learning for visual tracking," in *Proc. IEEE Int. Conf. Comput. Vis. (ICCV)*, Oct. 2017, pp. 2555–2564.
- [52] Q. Wang, Z. Teng, J. Xing, J. Gao, W. Hu, and S. Maybank, "Learning attentions: Residual attentional Siamese network for high performance online visual tracking," in *Proc. IEEE/CVF Conf. Comput. Vis. Pattern Recognit.*, Jun. 2018, pp. 4854–4863.
- [53] Z. Qiu, T. Yao, and T. Mei, "Learning spatio-temporal representation with pseudo-3D residual networks," in *Proc. IEEE Int. Conf. Comput. Vis. (ICCV)*, Oct. 2017, pp. 5533–5541.
- [54] S. Li, F. He, B. Du, L. Zhang, Y. Xu, and D. Tao, "Fast spatio-temporal residual network for video super-resolution," in *Proc. IEEE/CVF Conf. Comput. Vis. Pattern Recognit. (CVPR)*, Jun. 2019, pp. 10522–10531.
- [55] D. Tran, H. Wang, L. Torresani, J. Ray, Y. LeCun, and M. Paluri, "A closer look at spatiotemporal convolutions for action recognition," in *Proc. IEEE/CVF Conf. Comput. Vis. Pattern Recognit.*, Jun. 2018, pp. 6450–6459.
- [56] E. Ilg, N. Mayer, T. Saikia, M. Keuper, A. Dosovitskiy, and T. Brox, "FlowNet 2.0: Evolution of optical flow estimation with deep networks," in *Proc. IEEE Conf. Comput. Vis. Pattern Recognit.*, Jul. 2017, pp. 1647–1655.
- [57] S. Wanner, S. Meister, and B. Goldluecke, "Datasets and benchmarks for densely sampled 4D light fields," in *Proc. VMV*, 2013, pp. 225–226.
- [58] F. Chollet *et al.* (2015). *Keras*. [Online]. Available: <https://keras.io>
- [59] M. Abadi *et al.*, "Tensorflow: A system for large-scale machine learning," in *Proc. 12th USENIX Symp. Operating Syst. Design Implement. (OSDI)*, 2016, pp. 265–283.
- [60] D. P. Kingma and J. Ba, "Adam: A method for stochastic optimization," 2014, *arXiv:1412.6980*. [Online]. Available: <http://arxiv.org/abs/1412.6980>
- [61] M. Rerábek and T. Ebrahimi, "New light field image dataset," in *Proc. 8th Int. Conf. Qual. Multimedia Exper. (QoMEX)*, 2016, pp. 1–2.
- [62] *Stanford Lytro Light Field Archive*. Accessed: Apr. 13, 2019. [Online]. Available: <http://lightfields.stanford.edu/LF2016.html>



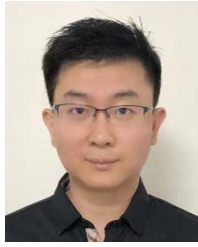
Zexi Hu received the B.S. degree in software engineering from South China Agricultural University, Guangzhou, China, in 2014, and the M.Phil. degree in engineering and IT from the University of Sydney, Sydney, NSW, Australia, in 2019.

He is an Invited Expert with the Multimedia Systems Lab, Beijing Technology and Business University (BTBU), Beijing, China. His research interests include computer vision and deep learning.



Henry Wing Fung Yeung received the M.Phil. and Ph.D. degrees in engineering and IT from the University of Sydney, Sydney, NSW, Australia, in 2017 and 2020, respectively.

He has authored or coauthored multiple international journal articles and conference papers, including the European Conference on Computer Vision and IEEE TRANSACTIONS ON IMAGE PROCESSING. His research interests include light field image processing and machine learning.



Xiaoming Chen received the B.Sc. degree from the Royal Melbourne Institute of Technology, Melbourne, VIC, Australia, in 2004, and the Ph.D. degree from the University of Sydney, Sydney, NSW, Australia, in 2009.

From 2010 to 2014, he was with the National University of Singapore, Singapore, CSIRO Brisbane, QLD, Australia, and IBM, Beijing, China. From 2014 to 2019, he was a Researcher with the Institute of Advanced Technology, University of Science and Technology of China, Hefei, China. In 2014, he was invited into the “100-Talent Program” by the Government of Hefei, Anhui Province, China. He is currently a Professor with the School of Computer Science and Engineering, Beijing Technology and Business University (BTBU), Beijing. Meanwhile, he has been invited as a Guest Researcher with Beijing Research Institute, University of Science and Technology of China, since 2019, and the School of Computer Science, University of Sydney. His research interests include immersive media computing, virtual reality, and related business information systems and applications. His work has been published in journals and conferences, including IEEE TRANSACTIONS ON IMAGE PROCESSING, IEEE TRANSACTIONS ON CIRCUITS AND SYSTEMS FOR VIDEO TECHNOLOGY, IEEE TRANSACTIONS ON BROADCASTING, IEEE TRANSACTIONS ON INSTRUMENTATION AND MEASUREMENT, IEEE MULTIMEDIA, ACM Multimedia, IEEE Virtual Reality, and European Conference on Computer Vision.



Yuk Ying Chung (Member, IEEE) received the B.S. degree in computing and information systems from the University of London, London, U.K., in 1995, and the Ph.D. degree in computer engineering from the Queensland University of Technology, Brisbane, QLD, Australia, in 2000.

From 1999 to 2001, she was a Lecturer at La Trobe University, Melbourne, VIC, Australia. She has been with the School of Computer Science, University of Sydney, Sydney, NSW, Australia, since 2001, where she is currently a Senior Lecturer. Her research

interests include image and video processing, virtual reality, deep neural network, machine learning, and data mining. Her work has been published in conferences and journals, including ECCV, NeurIPS, IEEE TRANSACTIONS ON IMAGE PROCESSING, and IEEE TRANSACTIONS ON CIRCUITS AND SYSTEMS FOR VIDEO TECHNOLOGY, and IEEE TRANSACTIONS ON CYBERNETICS.



Haisheng Li received the Ph.D. degree in computer graphics from Beihang University, Beijing, China, in 2002.

He is currently a Professor and Dean with the School of Computer Science and Engineering, Beijing Technology and Business University (BTBU), Beijing, China. His current research interests include computer graphics, scientific visualization, and 3-D model retrieval.